Fully Focused SAR Altimetry: Theory and Applications

Alejandro Egido, *Member, IEEE*, and Walter H. F. Smith

Abstract—In this paper, we introduce the concept, develop the theory, and demonstrate the advantages of fully focused coherent processing of pulse echoes from a nadir-looking pulse-limited radar altimeter. This process, similar to synthetic aperture radar (SAR) imaging systems, reduces the along-track resolution down to the theoretical limit equal to half the antenna length. We call this the fully focused SAR (FF-SAR) altimetry processing. The technique is directly applicable to SAR altimetry missions such as CryoSat-2, Sentinel-3, or Sentinel-6/Jason-CS. The footprint of an FF-SAR altimeter measurement is a narrow strip on the surface, which is pulse limited across track and SAR focused along track. Despite the asymmetry of the altimeter footprint, the fully focused technique may be useful for applications in which one needs to separate specific targets within highly heterogeneous scenes, such as in the case of sea ice lead detection, hydrology, and coastal altimetry applications. In addition, over rough homogeneous surfaces, such as the ocean or ice sheets, the improved multilooking capability of FF-SAR leads to a significant increase in the effective number of looks with respect to the delay/Doppler processing, resulting in better geophysical parameter estimation. The proposed processing technique was verified by processing full bit rate CryoSat-2 SAR mode data over the Svalbard transponder. Hydrology, sea ice, and open ocean applications are also demonstrated in this paper, showing the improvement of this technique with respect to conventional and delay/Doppler altimetry.

Index Terms—Altimetry, delay/Doppler altimetry, SAR altimetry, synthetic aperture radar (SAR).

I. INTRODUCTION

ONE of the main benefits of delay/Doppler altimetry is the improved resolution of the system along the satellite track [1], [2]. By means of an unfocused synthetic aperture radar (SAR) processing technique, the altimeter footprint along the flight direction can be reduced by an order of magnitude with respect to conventional altimeters. This has allowed resolving small-scale features on the ocean and providing altimetry data up to several hundreds of meters off the coast. The CryoSat-2 and Sentinel-3 European Space Agency (ESA) missions, which are operated in a closed burst mode, make use of coherent

A. Egido is with the Cooperative Institute for Climate and Satellites, University of Maryland, College Park, MD 20740 USA, and also with the Laboratory for Satellite Altimetry, National Oceanic and Atmospheric Administration, College Park, MD 20740 USA (e-mail: alejandro.egido@noaa.gov).

W. H. F. Smith is with the Laboratory for Satellite Altimetry, National Oceanic and Atmospheric Administration, College Park, MD 20740 USA (e-mail: walter.hf.smith@noaa.gov).

processing of the 64 echoes within each burst (aperture duration of about 3.5 ms), which allows narrowing the footprint in the direction along the track to about 300 m. The other main advantage is related to the improvement in the effective number of looks (ENL) due to the increase in the available number of independent samples to be multilooked [2], [3]. This has led to a significant improvement in geophysical parameter estimation for both the cryosphere [4] and the open ocean [5], [6].

In this paper, we introduce the notion, develop the theory, and demonstrate the advantages of fully focused coherent processing of pulse echoes from a nadir-looking radar altimeter. By accounting for the phase evolution of the scatterers in the scene, it is possible to focus along the track and perform an interburst coherent integration potentially during the entire illumination time of a scatterer on the surface [7]. We call this fully focused SAR (FF-SAR) altimetry. For the development of the technique, we have used the CryoSat-2 SAR mode full bit rate (FBR) data. However, this method is applicable to similar data from Sentinel-3 or Sentinel-6/Jason-CS, as it requires no hardware modifications as long as the radar altimeter preserves the coherency of the transmitted pulses during the target illumination time.

By applying the FF-SAR processing to a completely coherent target, the along-track resolution can be increased to its maximum theoretical limit, corresponding to half the antenna length. This was demonstrated by applying the FF-SAR technique to CryoSat-2 SAR mode data from transponder overpasses, obtaining an along-track resolution of 0.5 m. In the case of CryoSat-2 and Sentinel-3, the lacunar sampling obtained with the closed burst operation mode leads to sidelobes in the along-track point target response (PTR). However, this effect is not inherent in the FF-SAR processing technique. In fact, these sidelobes will be minimal in the case of Sentinel-6/Jason-CS, where the transmission of pulses is performed in a quasi-continuous fashion [8]. The sidelobes of the along-track PTR will have certain implications for the different applications of the technique, which are discussed in detail within this paper.

The footprint of the FF-SAR altimeter is a narrow strip on the surface, which is SAR focused along track and pulse limited across track. Despite the asymmetry of the footprint, the fully focused technique may be useful for applications in which one needs to differentiate targets within highly heterogeneous scenes, such as in the case of sea ice lead detection, inland water level determination, and coastal altimetry applications. For an extended surface such as the ocean, the FF-SAR altimeter waveform results from the combination of radar echoes from multiple scatterers on the surface. The resulting single looks of the ocean are random realizations of speckle noise. Repeating the

FF-SAR calculation using a new focal point at an along-track distance equal or greater than the resolution results in a new waveform that is independent of the previously calculated one. Thus, individual looks statistically independent from each other can be obtained from successive 0.5-m resolution cells. When incoherently averaged over a stipulated time interval, this method achieves the maximum number of looks available from SAR altimetry, thus maximizing the precision of subsequent measurements. It is also worth noting that the multilooked waveform is generated from infinitesimally narrow beams along track, resulting in a great simplification of the integrals involved in obtaining a theoretical expression for the statistically expected power.

Despite the fact that the possibility of focusing nadir-looking altimeter echoes had been previously suggested [9], we present here, for the first time, to the best of our knowledge, the theoretical derivation of the FF-SAR altimeter processing technique and the processing of real data. Fully focusing a nadir-looking altimeter has some similarities with classical aperture synthesis calculations in a traditional side-looking SAR imaging system. However, there are also significant differences, pertaining to the phase matching of the echoes along track, that need to be considered in detail. Thus, Section II reviews the mathematical derivations of the full deramping radar technique. Section III details the processing stages to achieve the FF-SAR waveforms. In Section IV, the two-dimensional PTR (2D-PTR) of such a system is discussed. Section V describes the properties of the multilook waveform that can be obtained out of the FF-SAR data. In Section VI, the validation of the technique over a transponder pass is reported. Section VII provides a description of some of the applications that are envisioned with this technique. Finally, Section VIII closes this paper with a discussion and concluding remarks.

II. PHASE OF DERAMPED PULSE ECHOES

In order to describe the FF-SAR altimetry processing technique, it is useful to start with the description of the transmitted and received radar echoes and the resulting signal after deramping. Despite the fact that the amplitude plays a nonnegligible role, particularly for the final signal-to-noise ratio and in the estimation of radar cross section (RCS), the phase is the essential feature of the signal for focused SAR processing. Therefore, we consider phase-only expressions in this analysis. With this assumption, each pulse transmitted by the radar can be mathematically described as [10]

$$s_t(t) = \exp\left(2\pi j \left(f_c \pm \frac{1}{2}\alpha t\right) t\right) \quad (1)$$

where f_c is the carrier frequency, t is the time varying within the pulse duration (the so-called fast time in radar literature), and α is the chirp rate, which is defined as B/T_p, with B being the chirp bandwidth and T_p being the pulse duration. It is assumed here that t runs from $-T_p/2$ to $T_p/2$. The plus or minus sign in the previous equation is a design consideration for the chirp slope. Hereafter, we consider for our derivation a negative chirp slope, as this is employed in most altimeter designs.

Without considering amplitude variations, after reflecting off a point scatterer on the Earth's surface, the received echo is a delayed and Doppler-shifted version of the transmitted one, which can be expressed as a function of fast time t and slow time η as

$$s_r(t, \eta) = \exp\left(2\pi j \left(f_c - \frac{1}{2}\alpha(t - \tau)\right)(t - \tau)\right) \quad (2)$$

where τ is the two-way travel time of the electromagnetic pulse, which is given by $\tau(t, \eta) = 2R(t, \eta)/c$, in which $R(t, \eta)$ is the range-to-target history, and c is the speed of light in vacuum. The dependence of τ on both t and η has been dropped from the previous equation for clarity. The Doppler shift is a consequence of the continuous motion of the platform during the transmission and reception of the chirp. The effects of the Doppler term, now implicit, will be evident further into the argument.

The deramp-on-receive technique is based on the analog mixing on board of the complex conjugate of the received signal with the replica of the transmitted pulse (matched filtering) [11]. In order to be able to observe the returned echoes, the copy of the transmitted signal needs to be delayed by a certain amount, i.e., d, based on the *a priori* knowledge of the range to the scatterer. In the case of the Synthetic Aperture Interferometric Radar Altimeter (SIRAL) instrument on board CryoSat, d is determined by the onboard tracker [12]. Defining τ' as $\tau' = \tau - d$, the resulting signal after deramping, i.e., the intermediate frequency or beat signal, yields

$$s_{\text{IF}}(t, \eta) = s_t(t - d) \cdot s_r(t, \eta)^*$$
$$= \exp\left(2\pi j \left(f_c \tau' - \alpha \tau' t + \frac{\alpha}{2}\tau'^2\right)\right). \quad (3)$$

The output of the mixer is then low-pass filtered before sampling. The beat signal is a continuous wave (CW) signal whose frequency is directly proportional to time delay, through the chirp rate, i.e., $f_b = \alpha \tau'$. The range compression is finally completed by performing a fast Fourier transform (FFT) after digitization.

In order to fully characterize the phase of the beat signal, let us consider now the evolution of τ' along slow time. Conventional radar processing algorithms assume that the platform is stationary during the transmission and reception of the radar pulses, i.e., stop-and-go approximation. However, the range to target $R(t, \eta)$ is in fact continuously changing due to the satellite's motion. For any given pulse transmitted at slow time η, the range to target as a function of fast time can be approximated as $R(t; \eta) \approx R(\eta) + v_r(\eta)t$, where $R(\eta)$ and $v_r(\eta)$ are the range and the relative velocity of the platform with respect to the scatterer at the center of the radar pulse, respectively. For the specific case of the radar altimeter, in which the duration of the transmitted pulse is on the order of tens of microseconds, the maximum error assuming this approximation is two orders of magnitude lower than 1 μm, which we can safely ignore.

The delay with respect to the tracker reference R_{trk} can be then written as

$$\tau'(t, \eta) = \frac{2(R(t, \eta) - R_{\text{trk}})}{c} \approx \tau'(\eta) + \frac{2v_r(\eta)t}{c}. \quad (4)$$
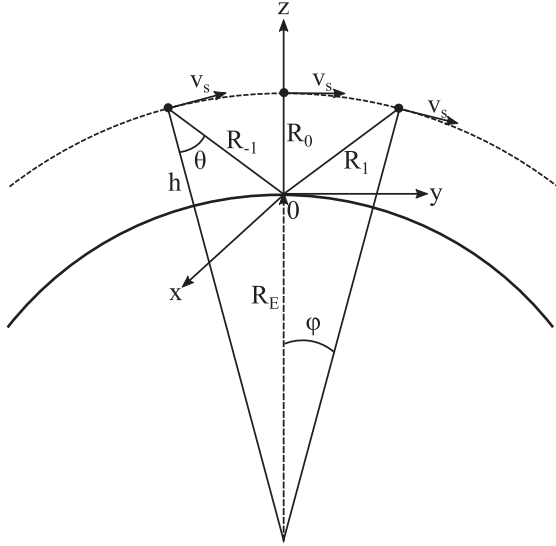
Fig. 1. Satellite altimetry observation geometry. The range of the satellite to the specular point at three different positions is shown, i.e., $R_{\{-1,0,1\}}$, corresponding to $\eta = \{\eta_{-1}, \eta_0, \eta_1\}$.

Substituting this expression into (3), we find that the phase of the beat signal is

$$\Phi(t,\eta) = 2\pi j \left(f_c \tau' - \left(\alpha \tau' - \frac{2 f_c v_r}{c} \right) t + \frac{\alpha}{2} \tau'^2 + \Phi_r \right) \quad (5)$$

where Φ_r represents the residual phase terms of the deramping process. It can be shown that, in our case, this term is always smaller than 0.01 rad, and therefore, it can be considered negligible. Note that the previous equation is very similar to the phase of (3); the only additional term is $2 f_c v_r / c$, which corresponds to the Doppler frequency shift due to the relative motion of the platform with respect to the target, which is denoted by $f_D(\eta)$. It is therefore appropriate to assume the stop-and-go approximation in this case, provided that the Doppler frequency shift is considered in the beat signal equation.

The effect of this additional term on the signal is a range displacement, since, as aforementioned, in the deramped signal, the range information is encoded in frequency components. This needs to be corrected in order to align the target response to a common reference range.

III. FOCUSED SAR PROCESSING

Given the deramp-on-receive design of radar altimeters, the FF-SAR altimetry processing is similar to Spotlight-SAR algorithms [13] used for imaging applications. In our case, the altimeter is pointed to nadir, and while the higher order phase terms are typically small and can be safely ignored in side-looking imaging systems [13], they need to be accounted for in our focused SAR processing. These terms are space variant for points at different positions across track. Thus, we are required to provide a suitable phase matching solution for all the scatterers within the antenna footprint. All these aspects are discussed in depth within this section.

The altimeter observation geometry is shown in Fig. 1. For convenience, it is assumed that the center of our Cartesian coordinate system is located at our focusing point, which can be arbitrarily chosen. For our derivation, we select the focusing point as the point of the closest approach to the Earth's surface, or the specular point. This condition determines $\eta = 0$. The satellite orbit at an altitude h over the Earth is contained in the yz plane. The x-axis completes the right-handed coordinate system and corresponds to the across-track dimension.

The specular point is observed during a period of time referred to as the target illumination time, i.e., T_{SAR}, which is determined by the 3-dB antenna beamwidth θ and the satellite velocity v_s. The range history of the ith scatterer on the surface, i.e., $R_i(\eta)$, can be defined as

$$R_i(\eta) = R_i + \delta R_i(\eta) \quad (6)$$

in which R_i is the minimum range to the target, and $\delta R(\eta)$ is the range migration as a function of slow time due to the platform movement as it flies over the scatterer. As shown in the previous section, the range migration incurs not only in a variation in the time of arrival of the radar echoes but also in a phase variation and a Doppler frequency shift. The main purpose of the focused SAR processing is to align both the delay and the phase history of the scatterers in the scene in order to coherently combine the radar echoes during a scatterer illumination time.

A. RCMC

Conventional SAR processing algorithms, such as the range–Doppler algorithm, make use of an along-track FFT that maps the response of the scatterers in the scene in the Doppler frequency domain, which allows applying the range cell migration correction (RCMC), using an unambiguous relationship between Doppler and range [10]. This technique is also used in delay/Doppler radar altimetry [1]. In our processing, we apply the RCMC for any point on the scene given the geometrical range variation during the target illumination time, in a similar way as the time-domain back-projection algorithm [14]. The delay history $\tau_i'(\eta)$ for the ith scatterer is

$$\tau_i'(\eta) = 2 \frac{R_i + \delta R_i(\eta) - R_{\text{trk}}}{c}. \quad (7)$$

Defining γ_i as the minimum two-way travel time to the target referenced to the tracker range, i.e.,

$$\gamma_i = 2 \frac{R_i - R_{\text{trk}}}{c} \quad (8)$$

we can write the delay history as

$$\tau_i'(\eta) = \gamma_i + 2 \frac{\delta R_i(\eta)}{c}. \quad (9)$$

The latter can be computed according to the satellite orbit positions provided in the data product. The satellite orbit positions are usually provided at a much slower rate than the pulse repetition frequency (PRF); hence, for the estimation of the geometrical range to target for every radar pulse, the geometrical range is interpolated according to a second-order or a fourth-order polynomial, depending on the required precision.

As shown in Appendix A, the two-way range migration difference between a scatterer located at nadir and a scatterer at an across-track position corresponding to the edge of the antenna beam is smaller than 4 mm during the whole illumination time. Therefore, for the RCMC, we can assume a single $\delta R(\eta)$ for all targets aligned on the same along-track position. For simplicity, we choose the point of the closest approach as the reference point for the RCMC.

Accounting also for the range displacement due to the Doppler frequency shift, as in (5), we can express the total range cell migration as $(\delta R(\eta) - c f_D(\eta)/\alpha)$. Applying the correction for the total range cell migration to (3), the resulting range cell migration corrected signal for the ith scatterer can be written as

$$s_{i,\text{RCMC}}(t,\eta) = s_{i,\text{IF}}(t,\eta) \exp\left(2\pi j \left(\frac{2\alpha\delta R(\eta)}{c} - f_D(\eta)\right) t\right)$$
$$= \exp\left(2\pi j \left(f_c \tau_i'(\eta) + \alpha\gamma_i t + \frac{\alpha}{2}\tau_i'(\eta)^2\right)\right). \quad (10)$$

The first term on the complex exponential represents the phase rotation due to range migration. We call this the relative range phase (RRP), which is the dominant phase term. Like the range evolution, the RRP follows a quasi-quadratic behavior. The second term is the CW phase, whose frequency is proportional to the minimum delay referenced to the tracker range, i.e., γ_i. This is the desired phase term as it determines the position of the target within the tracking window. The third term, commonly referred to in the literature as the residual video phase (RVP) [13], has a much less significant effect than the first one; however, in our case, it is strong enough to destroy the focusing and should be accounted for and corrected.

B. Range Compression

After RCMC, the range variations along slow time due to the relative movement of the platform and the focusing point are removed. However, in a real scenario, the actual radar signal is, in fact, the combination of multiple echoes coming from different targets in the scene. As will be explained in the following section, the next steps in the FF-SAR processing require the compression of the signal in range, in order to be able to apply the appropriate phase corrections to the complex radar data. Thus, taking a fast-time FFT to $s_{i,\text{RCMC}}$ to achieve range compression, we obtain that

$$S_{i,rc}(f_r,\eta) = \int_{\tau_i}^{\tau_i+T_p} s_{i,\text{RCMC}}(t,\eta) \exp[-j2\pi f_r t]dt$$
$$= T_p \text{sinc}\left[T_p(f_r - \alpha\gamma_i)\right] \exp[j\pi\Phi_{rc}] \quad (11)$$

where

$$\Phi_{rc} = 2f_c\tau_i'(\eta) + \alpha\tau_i'(\eta)^2 - 2(f_r - \alpha\gamma_i)\tau_i'(\eta) - (f_r - \alpha\gamma_i)T_p. \quad (12)$$

Given that the frequency components f_r can be directly linked to time delay through the simple relationship $f_r = \alpha\tau_r$,

and since $\text{sinc}[T_p(f_r - \alpha\gamma_i)]$ is strongly peaked around $\alpha\gamma_i$, (11) can be approximated as

$$S_{i,rc}(\tau_r,\eta) \approx T_p \text{sinc}\left[B(\tau_r - \gamma_i)\right]$$
$$\cdot \exp\left[j2\pi\left(f_c\tau_i'(\eta) + \frac{\alpha}{2}\tau_i'(\eta)^2\right)\right]. \quad (13)$$

We refer to $S_{i,rc}(\tau_r,\eta)$ as the range cell migrated complex radargram, where τ_r represents the time delay within the altimeter ranging window. From the previous equation, it is apparent that, after RCMC and range compression, the response of a single scatterer will be concentrated around a single window delay $\tau_{r,i} = \gamma_i$. This corresponds to the two-way travel time of the minimum distance to the scatterer at an across-track position x_i, which is referenced to the tracker range. The actual radar impulse response is not exactly a sinc function due to small phase noise distortions, which slightly impact sidelobe levels. However, in this analysis, we assume a perfect sinc impulse response.

C. RVP Correction

The next step in the FF-SAR processing entails the RVP correction. In the same way as for the range cell migration, we analyzed what would be the phase error in case the RVP and RRP terms are corrected for all across-track positions, considering a single target in the scene, i.e., the specular point. This analysis is provided in Appendix B. We observed that, unlike the previous case, there is not a single RVP correction that suits all the across-track points within the antenna beam, essentially due to the fact that targets with different across-track positions have different γ_i values, which leads to very different RVP variations along slow time.

However, as introduced earlier, after RCMC and range compression, the response of any target on the same across-track position is mapped around a single delay, i.e., $\tau_{r,i}$. In that situation, it is possible to apply a single range history, i.e., $\tau_i'(\eta)$, for the RVP correction by simply accounting for the position of the target within the complex radargram.

Applying the RVP correction to the RCMC complex radargram, the resulting signal can be then written as

$$S_i(\tau_r,\eta) = S_{i,rc}(\tau_r,\eta) \exp\left[-j2\pi\left(\frac{\alpha}{2}\tau_i'(\eta)^2\right)\right]$$
$$= T_p \text{sinc}\left[B(\tau_r - \gamma_i)\right] \exp\left[j2\pi(f_c\tau_i'(\eta))\right]. \quad (14)$$

The remaining phase term is the RRP, which is removed in the last stage of the coherent processing. As shown in the following section, this phase term is actually exploited to achieve the focused SAR along-track resolution.

D. Along-Track Focusing

The focused SAR along-track processing is achieved by coherently combining the echoes received from a certain target along its illumination time. For that, the RRP effect needs to be removed to avoid the decorrelation of the target response. As for the RVP correction, the RRP counterrotation is applied to

the range compressed signal according to $\tau_i'(\eta)$. As shown in Appendix A, there is a range cell migration difference of 4 mm between a scatterer at nadir and a scatterer at the edge of the antenna beam. At Ku-band, this corresponds to a phase error bigger than $\pi/4$ rad, which leads to a decorrelation of the signal. Thus, there is not a unique RRP correction for all the scatterers within the altimeter field of view.

However, by rearranging terms in (31), we can write the range history of the ith scatterer as

$$R_i(\eta) = \sqrt{R_0^2(\eta) + (R_i^2 - R_0^2)}. \tag{15}$$

Equation (15) allows computing in a straightforward way the range history of any scatterer in the same along-track position, as a function of the range history of the specular point, and its minimum range R_i, which is intrinsically linked to the scatterer across-track position. This allows us to apply the exact phase counterrotation to all the range frequency components of the RCMC complex radargram.

This result is significant as R_i can be then obtained directly from the relative position of the range frequency component $f_{r,i}$ with respect to the one of the specular point position, i.e., $f_{r,0}$, and the minimum range to the specular point, i.e., R_0, simply by

$$R_i = c\frac{f_{r,i} - f_{r,0}}{2\alpha} + R_0. \tag{16}$$

The determination of the position of the specular point within the waveform could be problematic in complicated scenarios when multiple bright scatterers are present in the scene, but in most cases, the specular point position is related to the point of minimum range within the tracking window.

Now, assuming that the RVP is correctly removed for the whole scene, after the RRP removal, the range and phase of all the echoes from a scatterer on the same along-track position as our focusing will be perfectly aligned. Finally, summing over the coherent processing time T_i yields the FF-SAR single-look complex (SLC) waveform, i.e.,

$$S_{i,\text{AT}}(\tau_r) = \sum_\eta S_i(\tau_r, \eta) \exp\left[-j2\pi\left(f_c\tau_i'(\eta)\right)\right]$$
$$= T_pT_i\text{sinc}\left[B(\tau_r - \gamma_i)\right]. \tag{17}$$

The final SAR image can be obtained by focusing on successive points along the satellite track.

IV. TWO-DIMENSIONAL PTR

To determine the along-track response of the FF-SAR altimetry, the focused coherent processing is applied at different positions along the track. The FF-SAR response for the ith scatterer, which is located at the specular point, evaluated at an along-track position y_a yields

$$S_{i,\text{AT}}(\tau_r; y_a) = \sum_\eta S_i(\tau_r, \eta) \exp\left[-j2\pi\left(f_c\tau_{y_a}'(\eta)\right)\right]$$
$$= T_p\text{sinc}\left[B(\tau_r - \gamma_i)\right] \sum_\eta \exp[j2\pi f_c\delta\tau']. \tag{18}$$

where $\delta\tau' = \delta\tau'(\eta) = \tau_i'(\eta) - \tau_{y_a}'(\eta)$. This equation reduces to (17) when $y_a = 0$. To obtain a closed analytical form of the 2D-PTR, $\delta\tau'$ is approximated as

$$\delta\tau'(\eta) = \tau_i'(\eta) - \tau_{y_a}'(\eta) \approx \frac{2y_ay - y_a^2}{cR_0} \tag{19}$$

where y represents the platform position along the orbit. It should be noted here that these approximations are not performed in the actual focused SAR processing, where the range to the target is determined by the position of the platform at every point in the orbit, but they are just adopted here for the analytical derivation of (19). Making this approximation and assuming that

$$\sum_{i\in I} f(i) \approx \int_I f(x)dx \tag{20}$$

we can write $S_{i,\text{AT}}(\tau_r; y_a)$ as

$$S_{i,\text{AT}}(\tau_r; y_a) \approx T_p\eta\text{sinc}\left[B(\tau_r - \gamma_i)\right]$$
$$\times \int_{-T_i/2}^{\frac{T_i}{2}} \exp\left[j2\pi f_c\frac{2y_a\eta v_s - y_a^2}{cR_0}\right] d\eta \tag{21}$$

where T_i is the coherent processing time. Evaluating the integral, we obtain

$$S_{i,\text{AT}} \approx T_p\text{sinc}\left[B(\tau_r - \gamma_i)\right] \exp\left[-j2\pi f_c\frac{y_a^2}{cR_0}\right] \frac{-jcR_0}{4\pi f_cy_av_s}$$
$$\times \left(e^{[j2\pi f_cy_av_sT_i/(cR_0)]} - e^{[-j2\pi f_cy_av_sT_i/(cR_0)]}\right)$$
$$\approx T_pT_i\text{sinc}\left[B(\tau_r - \gamma_i)\right]$$
$$\times \text{sinc}\left[T_i\frac{2f_cy_av_s}{cR_0}\right] \exp\left[-j2\pi f_c\frac{y_a^2}{cR_0}\right]. \tag{22}$$

Inspecting the previous equation, we find that the exponential phase term can be disregarded given that the second sinc function is strongly peaked around $y_a \approx 0$. Thus, the 2D-PTR can be written as

$$\chi_i(\tau_r, y_a) \approx T_pT_i\text{sinc}\left[B(\tau_r - \gamma_i)\right] \text{sinc}\left[T_i\frac{2f_cy_av_s}{cR_0}\right] \tag{23}$$

which can be also expressed as a function of the range and Doppler frequency f_D by considering that

$$\frac{2f_cy_av_s}{cR_0} \approx \frac{2v_s\sin(\phi)}{\lambda} = f_D \tag{24}$$

thus

$$\chi_i(\tau_r, f_D) \approx T_pT_i\text{sinc}\left[B(\tau_r - \gamma_i)\right] \text{sinc}\left[T_if_D\right]. \tag{25}$$

A. Across-Track Resolution

As in every chirp-based radar, the range resolution is determined by the chirp bandwidth. The two-way slant range power resolution is given by [10]

$$\delta R_\text{sr} = 0.886\frac{c}{2B} \tag{26}$$

where B accounts for the chirp bandwidth. In the same manner, we can also obtain the range resolution considering our 2D-PTR provided in (25): assuming $\gamma_i = 0$, the response in range yields a sinc whose half power is roughly obtained when $B\tau_r = \pm 0.886/2$; thus, the -3-dB power width of the sinc function in fast time is given by $\delta\tau = 1/B$, which yields the same result as before for the two-way slant range resolution in (26).

In order to determine the ability of the radar to differentiate two closely spaced targets on the surface, the slant range resolution needs to be projected on the ground. Indeed, the radar will be able to distinguish targets whose ranges differ more than δR_{sr}. Taking CryoSat-2 as an example, for example, $h \approx 730$ km and $B = 320$ MHz, due to the nadir-looking geometry of the altimeter, the ground range resolution of the first echo sample is 1600 m. The resolution increases approximately as the inverse of the square root of the delay with respect to the nadir point [1], [15]; thus, for the waveform tail, this is reduced to 50 m.

B. Along-Track Resolution

As in the previous case, the along-track resolution can be also directly derived from the 2D-PTR. From (25), we can write that the along-track sinc half power width is obtained when $T_i f_D = \pm 0.886/2$. Substituting f_D by its value, as specified in (24), and isolating y_a, we find that the along-track resolution δR_{az}, is

$$\delta R_{az} = 0.886 \frac{cR_0}{2f_c v_s T_i}. \qquad (27)$$

The maximum along-track resolution is achieved when the coherent processing is performed for the whole target illumination period T_{SAR}. This is ultimately determined by the antenna beam pattern along track. For large antennas, in comparison to the wavelength, the antenna beamwidth can be approximated as $\theta_a \approx 0.886\lambda/L_a$, where L_a is the length of the antenna in that particular dimension.

Projected on the ground, the antenna beam yields a footprint that can be approximated as $\theta_a R_0$, and therefore, the target illumination time can be written as $T_{\text{SAR}} = 0.886\lambda R_0/(L_a v_g)$, where v_g is the satellite velocity projected on the ground, that is, $v_g = v_s/\alpha_E$, with the orbital factor given by $\alpha_E = (R_E + 1)/R_E$. The maximum attainable along-track resolution yields $L_a/(2\alpha_E)$, corresponding to the maximum attainable resolution of a conventional spaceborne SAR system [10]. In the case of CryoSat-2, this is equal to approximately 0.5 m. As shown in (27), the along-track resolution is inversely proportional to the coherent processing time T_i. In some cases, it could be beneficial to reduce T_i in order to improve the processing time of the FF-SAR waveforms. However, this would be at the expense of along-track resolution and available number of looks.

It is also relevant to note here that if the coherent summation were performed burst by burst, the averaged echo ensemble would result in the delay/Doppler stack, where each of the coherently summed bursts would correspond to a Doppler beam after rocking the view angle to the focusing point. This is equivalent to the delay/Doppler processing approach presented in [16], which implies that, with the processing technique presented in this paper, we are able to obtain simultaneously the fully focused and delay/Doppler responses.

V. MULTILOOK WAVEFORM

In general, the waveform of a radar altimeter can be modeled as the convolution of the height distribution of the random rough surface under observation and the radar flat-surface response [17]. The latter is obtained as the convolution of the PTR, which accounts for the instrument's resolution across and along track, and the flat-surface impulse response (FSIR), comprising the effects of the antenna pattern, illumination geometry, and surface backscattering properties [1]. The only term in the model that is altered by the coherent processing is the flat-surface response function; thus, we will concentrate on this term for the analysis of the delay/Doppler and FF-SAR multi-looked waveforms.

To compare the flat-surface response of both systems, we computed numerically the power scattered off a quasi-flat surface for any time delay τ_r and Doppler beam f_n, the latter corresponding to different look angles along track [2]. The flat-surface response for the single Doppler beams can be obtained as the integral of the radar equation over the illuminated area, i.e.,

$$p_{\text{FS}}(\tau_r, f_n) = \frac{\lambda^2}{(4\pi)^3} \int\limits_A \frac{G^2(\vec{\rho})\sigma^0(\vec{\rho})\chi(\delta\tau_r, \delta f)}{R^4(\vec{\rho})} d\vec{\rho} \qquad (28)$$

where σ^0 is the surface normalized RCS, G is the antenna gain, and R is the distance to the scatterers on the surface, whose positions are determined by $\vec{\rho}$. As in the previous sections, χ represents the 2D-PTR of the system, which can be approximated as

$$\chi(\delta\tau_r, \delta f) \approx \text{sinc}[B\delta\tau_r]\text{sinc}[T_i\delta f] \qquad (29)$$

with $\delta\tau_r = \tau - 2R(\vec{\rho})/c$ and $\delta f = f_D(\vec{\rho}) - f_n$. In the previous equation, T_i represents the coherent integration time, which, in the case of the delay/Doppler processing, is the burst duration, and in the fully focused case, this value corresponds to the scatterer illumination time T_{SAR}.

Considering that σ^0 and R are both slowly varying within the illuminated area, we can assume that they are constant values for the integral; thus, the flat-surface response function can be approximated as

$$p_{\text{FS}}(\tau_r, f_n) \approx K \int\limits_A G^2(\vec{\rho})\chi(\delta\tau_r, \delta f) d\vec{\rho} \qquad (30)$$

where K is a constant, comprising the σ^0 and R terms. In order to ease the computation of the integral, the sinc functions of the 2D-PTR, as well as the antenna pattern, can be approximated by Gaussians [2], [18], whose widths can be related to the slant range and along-track resolutions, and the antenna beamwidth.

Due to the elliptical orbit around an ellipsoidal Earth, the satellite has a vertical velocity component that steers the zero-Doppler location away from nadir. In the delay/Doppler process, a compensation for vertical velocity is applied prior to the along-track FFT that forms the Doppler beams, so that the zero-Doppler beam is aimed at nadir. In the top panel in Fig. 2, we show the flat-surface response for the different beams of the delay/Doppler stack. Those have been Doppler corrected and range migrated to a common reference, i.e., the zero-Doppler beam. As the look angle with respect to nadir increases, the
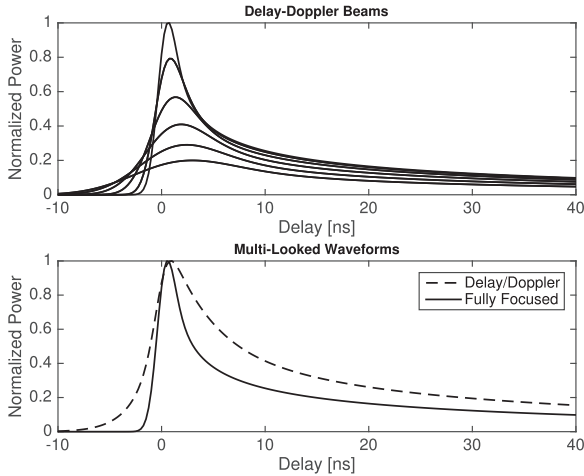
Fig. 2. (Top panel) Delay/Doppler flat-surface response for single Doppler beams at different look angles. (Bottom panel) Delay/Doppler and FF-SAR total flat-surface response.

active scattering area and the antenna gain decrease; thus, the amplitude of the outer beams is significantly lower than that of the central one. In addition, the energy of the outer beams is more spread than that of the nadir one, as the range of delays within each Doppler beam increases as the square of f_D [1], [2]. This has the effect of widening the total flat-surface response, which is obtained as the sum of all Doppler beams. As SAR focusing is referenced to the point of the closest approach, the FF-SAR flat-surface response corresponds to the delay/Doppler zero-Doppler beam, which results in a narrower flat-surface response, as shown in the bottom panel in Fig. 2.

As aforementioned, the final waveforms are obtained by convolving the FSIR with the surface height probability distribution. If the latter is the predominant one, as in the case of rough surfaces, then both waveforms will tend to be of the same width. However, for smooth surfaces, the FF-SAR waveform will tend to be sharper than the delay/Doppler one. This has two main advantages. First, as shown in [18], the narrower multilooked waveform results in sharper partial derivatives with respect to the model parameters, such as range to target and surface roughness. This leads to higher sensitivity, which could represent an improvement in the retracking performance, as aforementioned, in the case of smooth surfaces. Second, as also discussed in [18], the fact that the FF-SAR flat-surface response resembles the nadir-looking beam implies that the multilooked waveform can be straightforwardly modeled by a closed analytical form, thus simplifying the retracking process, whereas for the delay/Doppler case, all beams need to be computed individually to obtain the final multilooked waveform [2], [19].

The last point to consider regarding the multilooked waveforms of the delay/Doppler and FF-SAR altimeters involves the effective number of looks attainable by both systems. In the case of delay/Doppler altimetry, the multilooking is achieved by incoherently averaging the different Doppler beams of the stack [1], [2]. Due to the spreading of the waveforms in Doppler bins at increasing distance from nadir, the number of useful bins is significantly lower than the number of bins in the stack [20]. For the CryoSat-2 and Sentinel-3 configurations, this results in around 2700–3000 looks per second [2], [20], [21]. In the

case of FF-SAR, the multilooking is achieved by incoherently averaging the power of the SLC waveforms obtained by fully focused coherent processing at successive along-track positions. Assuming that the consecutive looks of the ocean surface, which are obtained at a spacing equal to the maximum along-track resolution, are independent from each other, with the CryoSat-2 configuration, one could achieve close to 14 000 looks per second [9]. However, as will be shown in Section VII-C, the ENL we obtain with CryoSat-2 SAR mode is roughly half that value due to the aforementioned lacunar sampling and sidelobes of the along-track PTR, as those introduce correlation in the successive SLC waveforms.

VI. VALIDATION OVER A TRANSPONDER

For the validation and demonstration of the FF-SAR altimetry processing, we used CryoSat-2 SAR mode data from transponder overpasses. The reason for selecting this particular type of data for the validation of our technique is that transponders act as point targets with high signal-to-noise ratio, which ultimately enabled us to evaluate the accuracy of the phase corrections. For this study, we used ESA FBR Baseline-B data. These data are uncalibrated, and therefore, CAL-1 and CAL-2 calibrations need to be applied prior to the FF-SAR processing. Here, we show the results for a descending track over the Svalbard transponder recorded on May 6, 2014.

The raw radargram for this track, as retrieved from the FBR data product, is shown in Fig. 3(a). For better visualization purposes, the original 128-element conventional waveforms of the SAR FBR product [22] were oversampled by a factor of 8 by zero-padding the digital samples of the complex echoes prior to the fast-time range FFT. For most passes over a transponder, the onboard tracker of the SIRAL instrument is set to a fixed value, and therefore, the tracker reference R_{trk} is constant throughout the whole track. This implies that all range and phase changes in the radar echoes are due to the geometrical range variation during the illumination period of the transponder. Thus, the parabolic shape of the range migration in slow time is clearly observed in the radargram. The returns at shorter range are related to surface clutter, as the spacecraft did not pass directly over the transponder. The across-track distance from the point of the closest approach to the transponder was determined to be 2.4 km. The returns at longer range are likely to be due to the other antennas and hard reflectors at the Svalbard transponder site.

The first step in the focused SAR processing is the RCMC. As discussed in Section III-A, a phase ramp in fast time is applied to remove the geometrical excess range with respect to the focusing point, in this case defined as the transponder location. The additional apparent delay caused by the Doppler frequency shift $f_D(\eta)$ was also accounted for and corrected. When both of these effects are compensated, the radargram is flattened out, as shown in Fig. 3(b) and (c). No residual slope is observed in the resulting radargram. The amplitude variations along the aperture due to the antenna pattern are also compensated according to the antenna beamwidth [16] and the pitch and roll information provided in the data product.

The phase of the radar echoes is obtained from the I and Q samples of the waveform maxima. In slow time, this signal
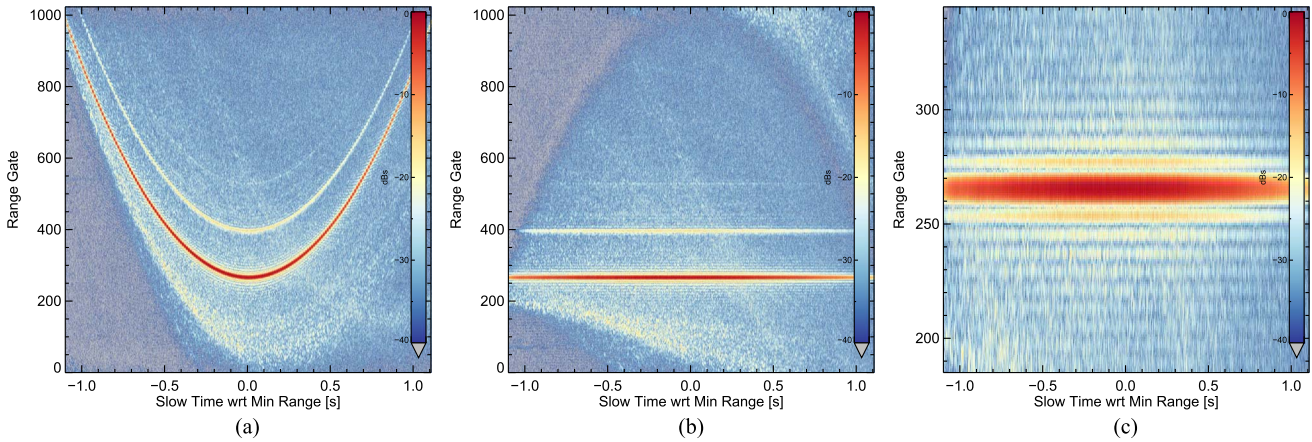
Fig. 3. (a) Power radargram for pass over the transponder. (b) Power radargram after geometrical RCMC. (c) Power radargram after geometrical RCMC (zoomed in). The sidelobes of the final sinc function in (26) are seen in the zoomed-in image in (c). The other bright streaks in (a) and (b) are due to other dish antennas near the transponder, which create additional bright targets in the scene.

follows the relationship introduced in (5) and (10). However, after correcting for the residual video phase and geometrical phase variations, as shown in Sections III-C and D, the phase of the echoes remains mostly constant. The standard deviation of the resulting phase is around $3°$, corresponding to a root-mean-square error in the round-trip phase of 0.2 mm at the radar carrier frequency.

At this point of the processing, the radar echoes are perfectly aligned in range and phase. The FF-SAR waveform is finally obtained by applying a coherent integration along the whole aperture. To obtain the 2-D impulse response, we performed the FF-SAR processing at successive points along the track. The 2D-PTR is depicted in Fig. 4(a), showing a 2-D sinc function centered at the transponder location. Taking the x and y cuts of this diagram at [0, 0] it is possible to obtain the across- and along-track responses, as shown in Fig. 4(b). The range waveforms were zero-padded to 4096 samples, to improve the waveform sampling. The slant range 3-dB width corresponds to the value attainable by the chirp bandwidth, as shown in (26). The along-track resolution is around 0.46 m, corresponding to the maximum attainable resolution by a SAR system [see (27)]. The latter result validates the FF-SAR processing for nadir-looking altimeters.

It should be noted here that, due to the closed burst operation of the CryoSat-2 and Sentinel-3 SAR altimeters, the along-track Doppler spectrum is not sampled uniformly. This lacunar sampling leads to sidelobes in the FF-SAR along-track PTR. In Appendix C, we introduce this issue more fully and provide a closed expression for the full along-track PTR. Despite the fact that this has certain implications in the application of the FF-SAR technique to CryoSat-2 and Sentinel-3 SAR mode data, we should stress that this issue is not inherent in the focused SAR processing and is solely due to the closed burst mode. In an open burst operation mode, such as the case of Sentinel-6/Jason-CS, the effect of these sidelobes will be minimal due to the quasi-continuous sampling of its interleaved operation mode [8] (with the only interruption of C-band and calibration pulses). Therefore, (25) is still valid as a general expression for the nadir-looking FF-SAR 2D-PTR.
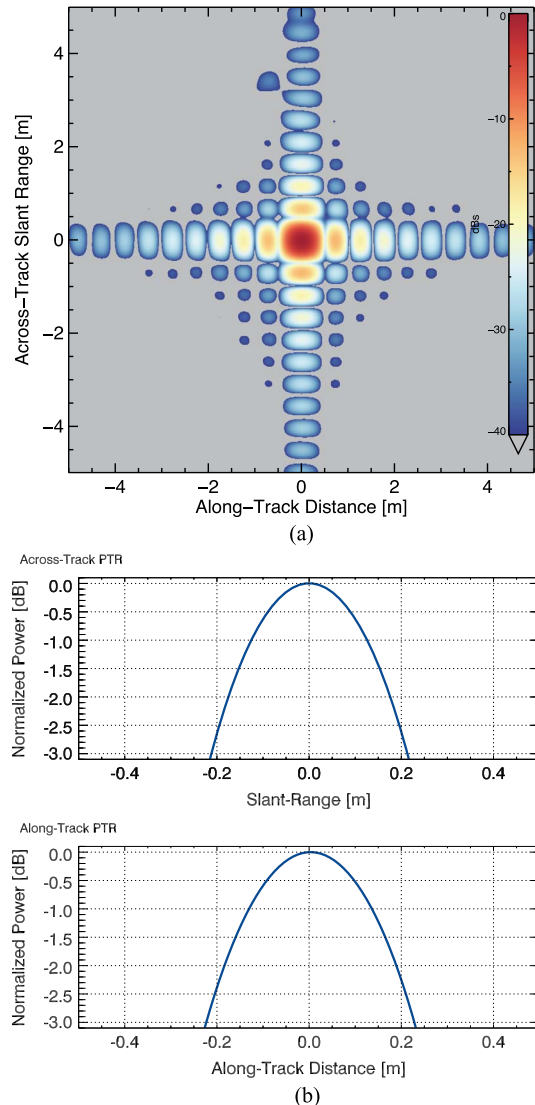

Fig. 4. (a) FF-SAR 2D-PTR obtained from CyroSat-2 FBR data from a transponder overpass. (b) (top panel) across-track PTR; (bottom panel) along-track PTR.

VII. APPLICATIONS

Here, we present a set of applications that could greatly benefit from the FF-SAR altimetry processing. Inland water, hydrology, and sea ice lead detection and freeboard applications will benefit from the improved along-track spatial resolution. Over the open ocean and ice surfaces, where backscatter is fairly uniform throughout the illuminated scene, incoherent multilooking of fully focused waveforms increases the ENL, and thus, one can trade higher spatial resolution for higher precision in range and surface roughness measurements. As a proof of concept for the FF-SAR altimetry processing technique, we provide next an introduction to some of the applications listed earlier.

A. Hydrology Applications

For the demonstration of the high-resolution applications, we tested the FF-SAR processing technique over small targets to assess the resolution with respect to the delay/Doppler processing. The FF-SAR processing was applied to a CryoSat-2 SAR mode track, recorded on June 8, 2010, over an active agricultural area in India with multiple artificial channels and small irrigation water reservoirs. Within this track, we identified a quasi-isolated square irrigation pond, which is located at (19.3715 N, 83.7902 W), of about 40 × 40 m, that lies very close to the subsatellite track of the altimeter.

In Fig. 5(a), we provide a Google Earth image of the area with the irrigation pond located at the center. From the image, we do not observe other significant targets that can contaminate the radar return from the pond. However, there is no imagery from June 10, 2010; thus, these assumptions are based on the Google Earth images collected at other times and the backscatter information obtained from the CryoSat data. In Fig. 5(b), we overlaid on the image the delay/Doppler response with a posting rate of 20 Hz as provided within ESA Baseline-B Level-1 b (L1 b) product [22]. The color scale represents the waveforms peak power normalized to the maximum power in the scene. The rectangular polygons are 300 m (along track) × 1600 m (across track), corresponding to the delay/Doppler along-track resolution and the first range gate across-track resolution projected on the ground.

In Fig. 5(c), we show the overlay of the FF-SAR response, which is obtained with an along-track resolution of 0.5 m and multilooked to 5 m. As can be observed, despite the fact that the sidelobes of the along-track PTR are visible, the along-track position of the pond and its extension can be clearly determined by the central lobe.

Since the along-track PTR is deterministic and has a closed mathematical expression (see Appendix C), in situations of high signal-to-clutter ratio, it is possible to apply standard deconvolution techniques to reduce the effect of sidelobes. Given its simplicity, for this study, we selected a constrained least squares (CLS) filter [23]. Applying the CLS deconvolution method to the FF-SAR along-track response, we obtain a significant reduction of the along-track PTR sidelobes, as shown in Fig. 5(d), which allows us to clearly determine the exact location and extent of the irrigation pond. This could be of great interest for a wide variety of hydrological studies, including flood extent monitoring.
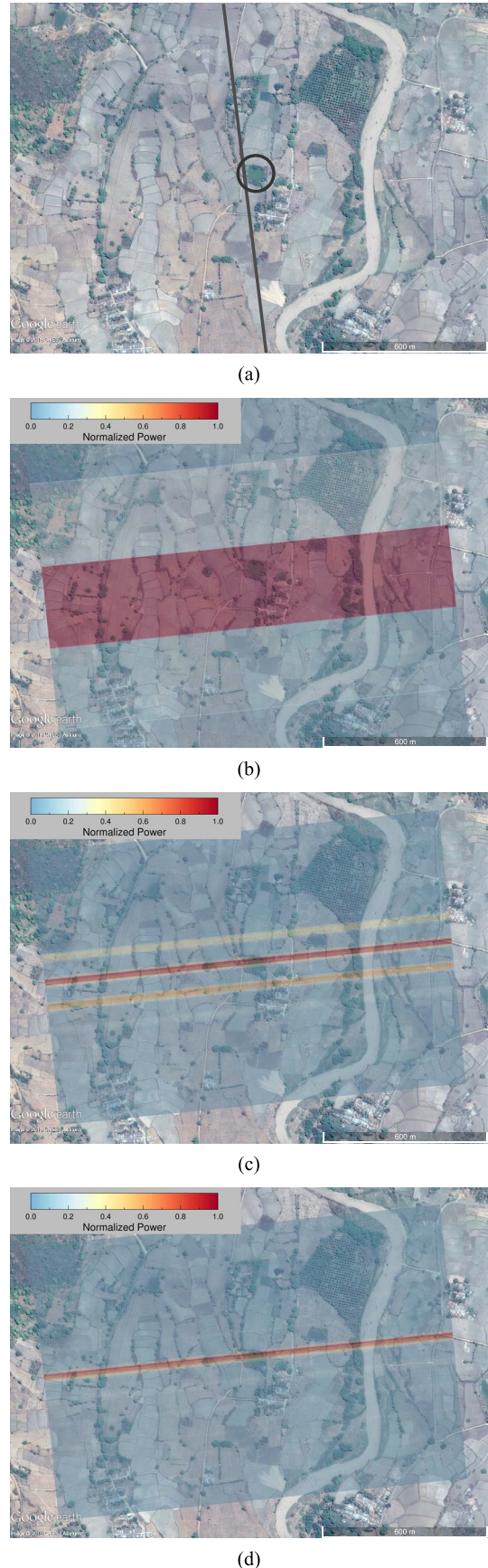

(a)

(b)

(c)

(d)

Fig. 5. (a) Google Earth image showing the small irrigation pond, encompassed by a circle, and the subsatellite track, depicted as a gray line. (b) Delay/Doppler response. (c) FF-SAR response. (d) FF-SAR response after deconvolution.

B. Sea Ice Applications

A similar analysis was performed over sea ice. In this case, we compared CryoSat-2 observations to data from the Digital Mapping System (DMS) on board the IceBridge NASA mission [24]. For this analysis, we selected a CryoSat-2 underflight performed on March 28, 2012. Within this track, we identified an area with recently formed sea ice leads. The FBR data of this track were processed by means of the FF-SAR processing technique, at an along-track resolution of 0.5 m. In order to compare our results directly to the official ESA products, we applied an along-track multilooking of 320 m, corresponding to a posting rate of roughly 20 Hz.

In Fig. 6(a), we show the power variations retrieved from the multilooked FF-SAR waveforms overlaid on the DMS geolocated and orthorectified images. For better visualization, the data were represented in polar-stereographic coordinates. The CryoSat and DMS data were acquired with a time difference under 1 h apart from each other; therefore, the ice drift is not significant for the type of analysis considered here. The along-track power variations are represented in color scale, setting in this case the 0-dB reference for the power measure from an extended ice surface (between 13 and 2 km south from the center of the image). After multilooking, the FF-SAR altimeter footprint is considered as a rectangle of 320 (along-track) × 1500 m (across-track), corresponding to the first waveform range gate projected on the ground. As observed from the image, as well as for the irrigation pond, the different features in the surface are clearly detected by the measured power variations, with a dynamic range of more than 30 dB.

In this application example, we also estimated the sea surface height (SSH) from the FF-SAR multilooked waveforms retrieved over sea ice leads. The sea ice lead positions were determined according to the surface classification method presented in [25], which is based on the pulse peakiness, and the delay/Doppler stack standard deviation. These two parameters were retrieved from the ESA L2 and L1 b products. For the estimation of SSH over leads, we implemented a simple waveform peak power parabolic retracker; as sea ice leads act, mostly, as specular scatterers, it suffices to determine accurately the position of the waveform peak in order to obtain a precise estimation of the range to the surface. In order to compare the FF-SAR and ESA L2 measurements, we removed the geoid variations and a constant bias between both data sets. Therefore, for the span of the observation area considered here, the mean sea surface is centered around 0.

The results are shown in Fig. 6(b). The sea ice lead positions are highlighted in light blue in the figure, corresponding very accurately to the sea ice leads observed in the DMS images. The individual SSH measurements in leads are shown for both the FF-SAR and ESA L2 products, as well as the mean SSH in the lead as determined by each measurement method, along with the 1σ uncertainty in the mean. The latter are computed as the standard deviation of the SSH measurements divided by the square root of the number of available measurements within each lead, which is, in all the cases, the same for both FF-SAR and ESA L2. It should be noted that the associated errors for the FF-SAR measurements are consistently lower than those for the ESA L2 product. In addition, the standard deviation of the SSH
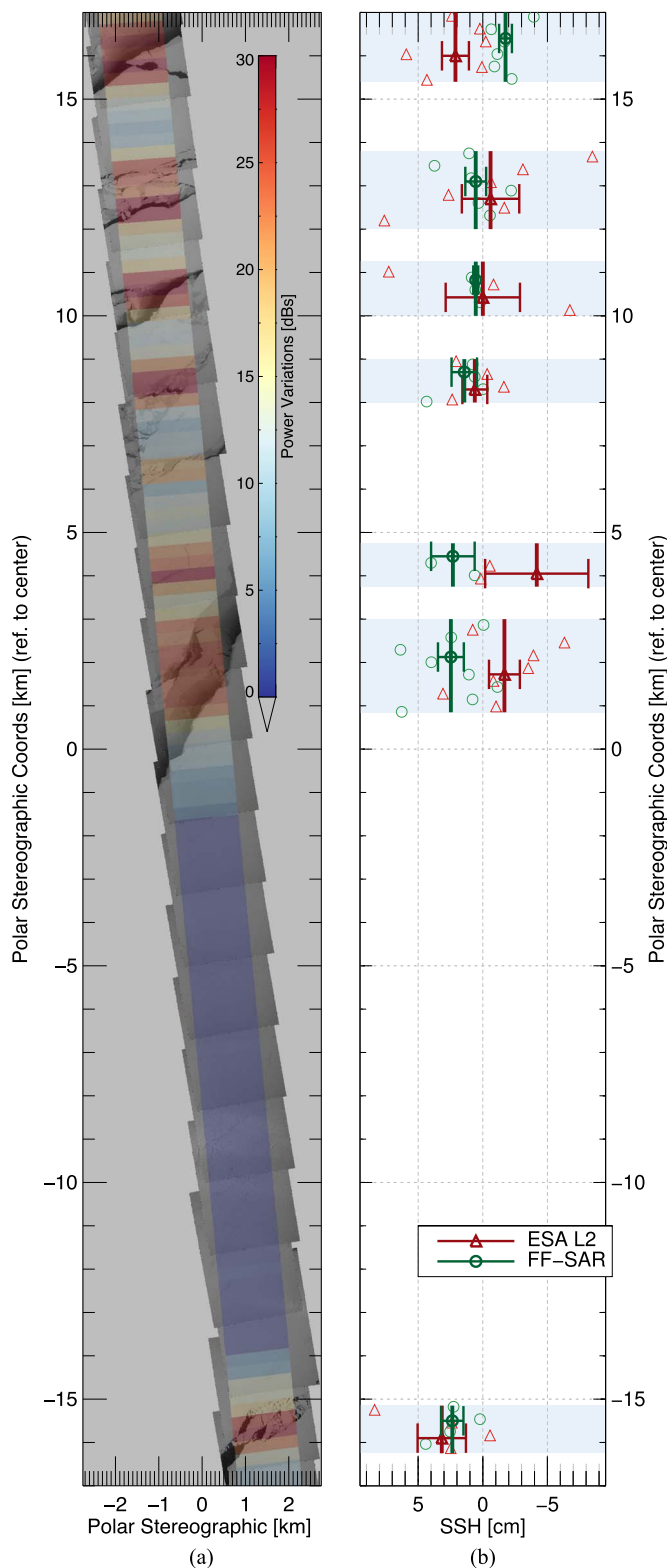

Fig. 6. (a) Sigma-0 measurements from CryoSat-2 FF-SAR data, processed at full resolution, with an along-track multilooking of 30 m. The sigma-0 measurements, represented in color scale, are overimposed to NASA IceBridge DMS geolocated images. (b) Comparison of ESA L2 (dark red) product and FF-SAR (dark green) SSH estimations over sea ice leads. The sea ice lead positions are highlighted in light blue. The single ESA L2 and FF-SAR measurements are represented with triangles and circles, respectively. The solid lines with the associated error bars correspond to the mean and the uncertainty of the height measurements for each sea ice lead identified in the scene.
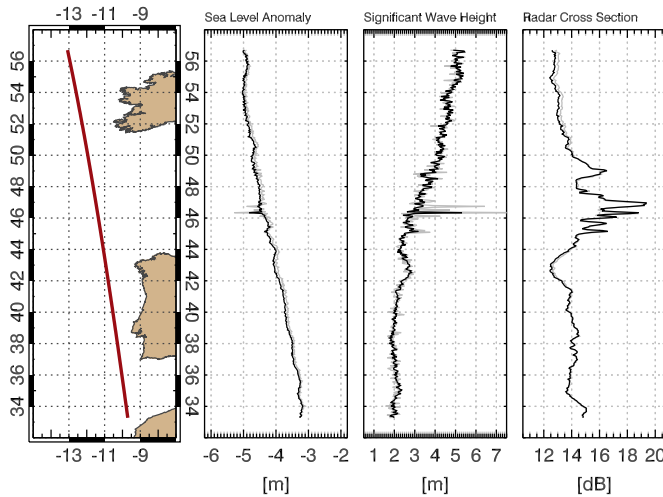
Fig. 7. CryoSat-2 SAR mode track over the North-East Atlantic. The panels show the satellite track and the geophysical parameters retracking results for both the PLRM (in gray) and FF-SAR (in black) data at 1 Hz.

measurements for the whole observation area considered here is reduced by a factor of $\sqrt{2}$, from 4.4 cm, for the ESA L2 product, to 3 cm for the FF-SAR estimations. As will be discussed in the following section, this improvement in the SSH retrieval is related to an increase in the ENL of the surface.

C. Open Ocean Applications

The FF-SAR processing was also applied to CryoSat-2 SAR mode data over the open ocean. Despite the fact that we expected the ocean to decorrelate after a short period of time, i.e., much shorter than the time required to form the synthetic aperture [26], we determined that a significant amount of power is left after the fully focused coherent processing.

To assess the performance of FF-SAR altimetry over the ocean, we used a CryoSat-2 SAR mode track over the Northeast Atlantic, which was recorded on January 7, 2012, at 22:52:27. This track was selected given its large latitude coverage, i.e., from 33° to 57° north, and the high variability in significant wave height (SWH), ranging between 2 and 6 m. The sub-satellite track is shown in the first panel in Fig. 7. As in the previous cases, the SAR focusing was performed at an along-track resolution of 0.5 m. The SLC observations were then multilooked over 320 m to make the resulting data directly comparable with ESA L1 b data product [22]. In order to make a fair comparison between both data sets, the antenna pattern was not compensated in this analysis. For completeness, the track was also processed by means of the unfocused SAR processing, as introduced in Section IV-B, with only a single focusing point at the center of the radar cycle to emulate the delay/Doppler process.

The FF-SAR waveforms were retracked by means of the SAR altimeter waveform analytical model described in [19] (so called, the SAMOSA model) [19] to obtain the standard geophysical parameters over the ocean, i.e., sea level anomaly (SLA), SWH, and RCS. As explained in Section V, in the FF-SAR case, only the nadir-looking beam needs to be considered to model the multilooked waveform, whereas for
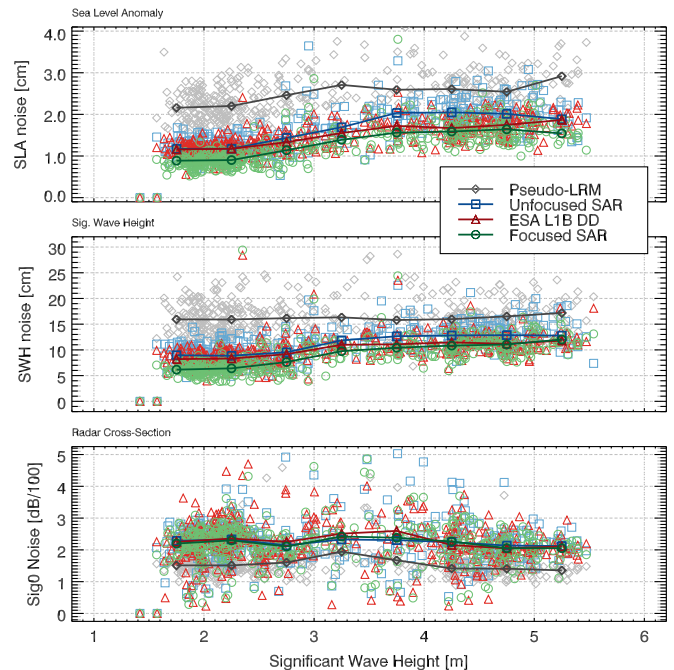

Fig. 8. Comparison of 1-Hz noise estimates for SLA, SWH, and RCS as a function of SWH, for the PLRM, unfocused SAR, and FF-SAR processing approaches.

the delay/Doppler and unfocused SAR processing, the full stack model has to be used. This is relevant as the waveform retracking processing time drastically decreases in the FF-SAR case.

The retracking outputs of the FF-SAR waveforms were compared to the pseudo low resolution mode (PLRM) [27] data from the Radar Altimetry Database System (RADS) [28], which provides consistent results with respect to the reference missions [29]. The geophysical parameters obtained from the FF-SAR and the RADS are provided in the second to the fourth panels in Fig. 7, in black and gray, respectively. As can be observed, apart from minor discrepancies, the estimated geophysical parameters for both processing approaches are largely coincident, which demonstrates that reliable ocean geophysical parameters can be retrieved by means of the FF-SAR processing. The cause for the second-order discrepancies between estimations will be investigated in future studies.

We also analyzed the precision in the geophysical parameters estimation for the different processing approaches. In Fig. 8, we show the 1-Hz noise estimates for SLA, SWH, and RCS, as a function of SWH, for PLRM, unfocused SAR, ESA L1 b official product, and FF-SAR. The 1-Hz noise values were computed as the standard deviation of the retracked geophysical parameters at 20 Hz within 1 s. The performance curves (solid lines in the plots) were then obtained as the median for SWH bins of 0.5 m.

The precision improvement of the SAR processing methods with respect to PLRM is clearly noticeable from the plot. This improvement amounts to a factor of 2 in SLA and SWH for both the unfocused SAR and the ESA L1 b product. In the case of RCS, PLRM presents higher precision than the other methods. These findings are consistent with the results obtained in previous studies [6]. As can be observed from the plots, for an SWH
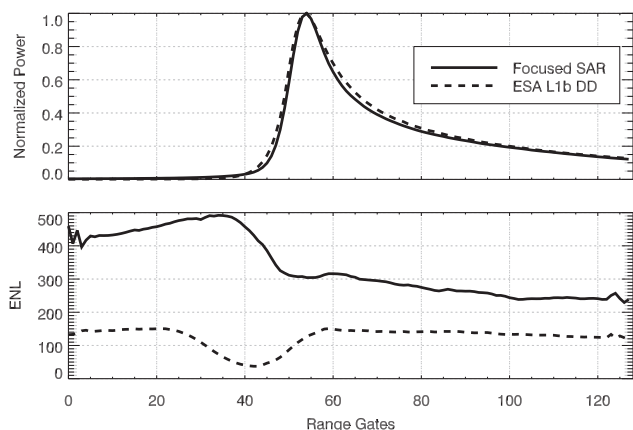
Fig. 9. (Top panel) Delay/Doppler and FF-SAR multilooked waveforms and (bottom panel) ENL at 20 Hz for an SWH of around 2 m.

of around 2 m, the unfocused SAR and the ESA L1 b product yield very similar results, indicating that both methods are essentially equivalent. Toward higher SWH values, ESA L1 b has better precision. The reason for this is attributed to the different processing options in the ESA L1 b processor before multilooking, such as Hamming windowing, which could lead to a more precise estimation of geophysical parameters.

In addition, there is also a significant precision improvement in the estimation of SLA and SWH of the FF-SAR with respect to the unfocused SAR methods. In the case of SLA, for an SWH value of 2 m, the performance improvement corresponds to a $\sqrt{2}$ factor with respect to the unfocused SAR and the ESA L1 b product. In fact, this ratio is maintained over all SWH ranges when comparing the unfocused and focused SAR, where the same processing options are applied. For SWH, the precision improvement is also $\sqrt{2}$ for SWH values up to 3 m and decreases afterward. Finally, in the case of RCS, all SAR methods present very similar performances.

As introduced earlier, the reason for the noise reduction in the estimation of geophysical parameters lies in the increase of the ENL of FF-SAR with respect to delay/Doppler, as suggested in [20]. The average waveforms and the ENL computed from the ESA L1 b and FF-SAR waveforms are shown in Fig. 9. Those were obtained for an SWH of around 2 m. As shown in the top panel in Fig. 9, the waveforms were shifted to a common reference point before averaging in order to be able to directly compare the results. From this plot, we also notice that the focused SAR waveform is narrower than the delay/Doppler case as the former does not include the widening effect of the outer Doppler beams of the stack. In the bottom panel in Fig. 9, the ENL of the 20-Hz multilooked waveforms is shown, demonstrating that, for the main part of the waveform, the ENL of the FF-SAR increases by a factor of 2 with respect to the delay/Doppler processing. This matches the reduction of a factor of $\sqrt{2}$ in the noise of the geophysical parameters.

Despite this improvement, it should be noted here that the increase in ENL is lower than expected for FF-SAR; the 320 looks obtained for the 20-Hz multilooked waveforms correspond to 6400 looks per second, less than half of the looks expected for FF-SAR. As introduced in Section V, this is linked to the la-

cunar sampling of the CryoSat-2 closed burst operation, which introduces sidelobes in the full along-track PTR, creating correlation between successive looks and, ultimately, decreasing the ENL. The pulse chronogram for Sentinel-6/Jason-CS will transmit Ku-band pulses almost continuously, except for occasional C-band and calibration pulses [8]. This will eliminate the lacunar sampling and therefore will eliminate the sidelobes in the along-track PTR. However, the Sentinel-6/Jason-CS PRF will be lower than the CryoSat and Sentinel-3 PRF by about a factor of 2, and thus, about half of the Doppler bandwidth will be aliased. The FF-SAR technique can be only applied to an unaliased Doppler bandwidth, which means, in practice, that the total available aperture length will be reduced by about half, and thus, the along-track PTR will be widened by a factor of 2, to about 1 m along track. This will prevent the achievement of the FF-SAR altimeter maximum performance for which a Nyquist sampled open burst SAR mode altimeter would be necessary.

Further analyses that fall outside the scope of this paper, with extended data sets and different processing options, are necessary to determine the actual performance of the FF-SAR over the open ocean. However, this study already suggests that, for low-resolution applications, the FF-SAR technique achieves a higher number of statistically independent looks, leading to an improved performance in the estimation of geophysical parameters.

VIII. Conclusion

FF-SAR altimetry represents a novel approach to the processing of nadir-looking radar altimeter pulse echoes. The technique we propose in this paper is based on SAR imaging back-projection algorithms with the relevant modifications to account for the altimeter nadir-looking geometry. The technique is applicable to any SAR altimeter as long as the radar is coherent.

Essentially, the FF-SAR altimeter waveform is obtained by performing a coherent integration of the altimeter echoes along the entire illumination time of a scatterer on the surface after SAR focusing, i.e., after compensating for the range and phase migrations with respect to the scatterer's position. The achievable along-track resolution then coincides with the theoretical limit of SAR imaging systems, equal to half the antenna length. For typical SAR altimeters, this corresponds to about 0.5 m, in contrast to the approximately 300-m resolution of the unfocused delay/Doppler processing.

In this paper, we have demonstrated the FF-SAR processing technique using CryoSat-2 FBR SAR mode data. The achievable along-track resolution was verified by processing data from transponder overpasses. Several applications have been also worked to demonstrate the use of FF-SAR. In hydrology and sea ice applications, the improved along-track resolution can be exploited to obtain a better representation of the surface features. In addition, we showed that the SSH estimations from sea ice leads can be improved with respect to the ESA L2 product due to the higher multilooking capabilities of FF-SAR. We also demonstrate the use of the technique for the open ocean, where a similar result is obtained. In this case, we

determined that the ENL of the multilooked echoes increases by a factor of 2 with respect to delay/Doppler, leading to a significant improvement in the estimation of the ocean geophysical parameters. The increase in ENL is lower than expected for an ideal FF-SAR as the closed burst operation mode of the CryoSat-2 SIRAL instrument imposes a lacunar sampling of the Doppler spectrum. This results in sidelobes in the full along-track point target response, which introduces correlation in the successive looks of the ocean. Sentinel-6/Jason-CS will avoid the lacunar sampling and the sidelobes, but it does not have an ideal PRF, and thus, we expect it to achieve only a 1-m along-track FF-SAR resolution. This effect could be mitigated by an open burst operation mode, with a high enough PRF to sample the whole Doppler spectrum.

The FF-SAR processing technique could be also applied to an interferometric altimeter. CryoSat-2's SARIn mode supplies such data, but with a lacunar sampling four times worse than CryoSat-2's SAR mode, and thus, we have not investigated this possibility. However, the FF-SAR processing applied to an open burst interferometric altimeter would provide a very valuable data set for a wide range of altimetric applications, particularly for ice studies.

APPENDIX A
RANGE CELL MIGRATION ANALYSIS

Referring to the altimeter geometry shown in Fig. 1, the range to a target at an across-track position x_i varies with slow time η as

$$R_i(\eta) = \sqrt{x_i^2 + y(\eta)^2 + z(\eta)^2}. \tag{31}$$

Due to the eccentricity of the orbit and the ellipsoidal shape of the Earth, the horizontal and vertical components of the satellite velocity are not constant. When we perform our FF-SAR processing, it is therefore necessary to use the actual orbit ephemeris data given in the FBR data product to determine $R_i(\eta)$ for one particular value of x_i.

However, to analyze how (31) varies with η as x_i changes, it suffices to assume that the satellite velocity components are constant for the whole illumination time. We assume that the subsatellite point on the ellipsoid moves forward at a steady rate $R_E\dot{\phi}$, where $\dot{\phi}$ is a uniform rotation along a circular arc approximating the nadir path in the Earth's surface, and the satellite's height above this circle changes steadily at a rate $\dot{h}$. The satellite position in our coordinate system can be then expressed as a function of the slow time, i.e.,

$$y(\eta) = (R_E + h + \dot{h}\eta)\sin(\dot{\phi}\eta)$$
$$z(\eta) = (R_E + h + \dot{h}\eta)\cos(\dot{\phi}\eta) - R_E. \tag{32}$$

We analyze here the range migration undergone by a scatterer at the edge of the swath with respect to the range migration of a scatterer at nadir. For that, we evaluate (31) with the following standard parameters: $h = 730$ km and $v_s = 7.5$ km/s. For the vertical velocity, we assumed a worst case value of 35 m/s, as the actual $|\dot{h}|$ is smaller than 35 m/s 99% of the time.
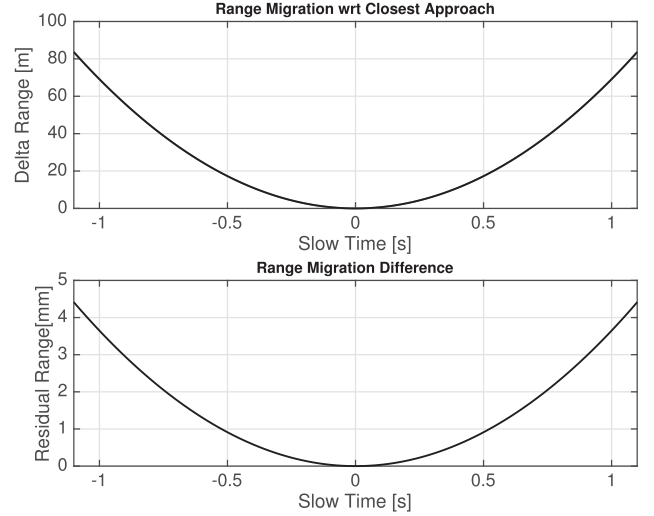

Fig. 10. (Top panel) Range cell migration for two targets with different across-track positions, i.e., nadir and antenna beam edge. (Bottom panel) Range cell migration difference between across-track targets.

The top panel in Fig. 10 depicts the range migration for an illumination time of 2 s, for a target at nadir and at the edge of the antenna beam, $x_i = 7500$ m. The bottom panel in Fig. 10 shows the difference between both range variations, showing a residual for the two-way travel distance lower than 4 mm for the whole illumination time. This implies that the RCMC can be applied as a single operation for each radar echo as scatterers on the surface with different across-track positions experience very similar range cell migrations.

APPENDIX B
RVP ANALYSIS

The RVP for the ith scatterer can be expressed as

$$\text{RVP}_i(\eta) = \pi\alpha\tau_i'^2(\eta) = \frac{4\pi\alpha}{c^2}\left(R_i + \delta R_i(\eta) - R_{\text{trk}}\right)^2. \tag{33}$$

From the previous equation, it can be inferred that the tracker range R_{trk} plays an important role on this parameter. In the top panel in Fig. 11, we present the RVP variations during the illumination time of a target located on the subsatellite track, i.e., across-track position $x = 0$. The RVP is shown for four different cases of tracker range with respect to the minimum range to target R_i. As can be seen, even in the case in which $R_{\text{trk}} = R_i$, the excursion of the RVP during the illumination time is large enough to hamper the coherency of the signal. However, the effect is even more significant when there is a discrepancy between the tracker range and the minimum range to target.

This discrepancy between the tracker range and the minimum range becomes apparent for targets far away from the subsatellite track, as the minimal range to the ith target increases with the across-track position. This makes it unfeasible to apply a single RVP correction for all the targets.

Nevertheless, if the discrepancy between the tracker range and the minimum range to target is accounted for and corrected when computing the RVP, then the RVP can be estimated as

$$\widetilde{\text{RVP}}_i(\eta) = \frac{4\pi\alpha}{c^2}\left(R_i + \delta R_0(\eta) - R_{\text{trk}}\right)^2 \tag{34}$$
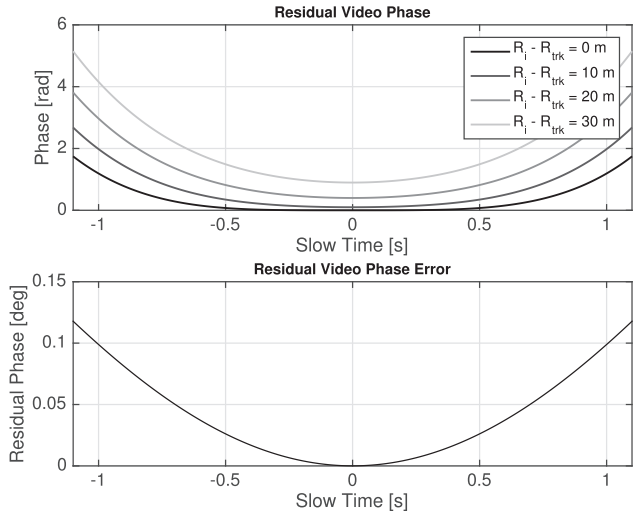
Fig. 11. (Top panel) RVP for four different trackers and minimum range to target situation, $R_{\text{trk}} = R_i$. (Bottom panel) RVP error between two across-track target positions, i.e., nadir and antenna beam edge.

Fig. 12. Unfocused and fully focused SAR extended along-track PTR measured from a transponder overpass.

where $\delta R_0(\eta)$ is the range migration for a target on the sub-satellite track.

In the bottom panel in Fig. 11, we show the error between $\widetilde{\text{RVP}}_i(\eta)$ and $\widetilde{\text{RVP}}_i(\eta)$ for a target at an across-track position $x = 7500$ m. It is observed that the maximum error for the whole illumination time is smaller than $0.1°$, which is considered to be negligible.

APPENDIX C
CRYOSAT-2/SENTINEL-3 FULL ALONG-TRACK RESPONSE

In order to accommodate the high PRF, the transmitted radar echoes are arranged in bursts of 64 pulses. The burst are 3.5 ms long with a burst repetition interval (BRI) of roughly 12 ms [16], which implies that, virtually, for more than two thirds of the time, the radar is not transmitting any signal; thus, the along-track Doppler spectrum is not uniformly sampled. This leads to sidelobes in the full along-track PTR, which are spaced according to the BRI. This effect is well known for ScanSAR imaging systems. The full along-track PTR can be written as [30]

$$h(y_a) = h_{\text{burst}}(y_a) \cdot \frac{1}{BP} \sum_n h_{\text{full}}\left(y_a - \frac{n}{BP}\right) \quad (35)$$

where h_{burst} represents the impulse response of the single burst, i.e., the delay/Doppler response, h_{full} is the impulse response of the full Doppler bandwidth, and BP is defined as the spectral burst cycle period, i.e., $BP = |FM| \cdot BRI$, with FM as the Doppler frequency rate.

For the SIRAL instrument and the CryoSat platform height and velocity, the FF-SAR along-track PTR is a series of 0.5-m-wide sinc functions, which are spaced roughly every 88 m and tapered by an envelope that corresponds to the delay/Doppler PTR, i.e., a sinc function whose main beamwidth is approximately 300 m. This has been verified by computing the extende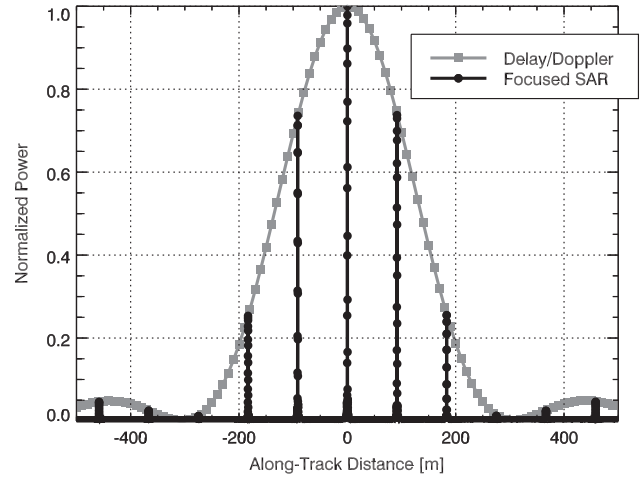d along-track response over the Svalbard transponder for both the unfocused and fully focused SAR processing. These results are shown in Fig. 12.

The multiple sidelobes in the along-track PTR will have an impact in some of the applications of the FF-SAR processing, particularly in the high-resolution ones. However, since the full along-track response is well known, deconvolution techniques can be applied to minimize this effect.

ACKNOWLEDGMENT

REFERENCES

[1] R. K. Raney, "The delay/Doppler radar altimeter," *IEEE Trans. Geosci. Remote Sens.*, vol. 36, no. 5, pp. 1578–1588, Sep. 1998.

[2] D. J. Wingham, L. Phalippou, C. Mavrocordatos, and D. Wallis, "The mean echo and echo cross-product from a beam forming, interferometric altimeter and their application to elevation measurement," *IEEE Trans. Geosci. Remote Sens.*, vol. 42, no. 10, pp. 2305–2323, Oct. 2004.

[3] R. K. Raney, "CryoSat SAR-mode looks revisited," *IEEE Geosci. Remote Sens. Lett.*, vol. 9, no. 3, pp. 393–397, May 2012.

[4] R. L. Tilling, A. Ridout, A. Shepherd, and D. J. Wingham, "Increased Arctic sea ice volume after anomalously low melting in 2013," *Nature Geosci.*, vol. 8, pp. 643–646, 2015.

[5] L. Phalippou and V. Enjolras, "Re-tracking of SAR altimeter ocean power-waveforms and related accuracies of the retrieved sea surface height, significant wave height and wind speed," in *Proc. IEEE IGARSS*, Jul. 23–28, 2007, pp. 3533–3536.

[6] L. Fenoglio-Marc *et al.*, "The German Bight: A validation of CryoSat-2 altimeter data in SAR mode," *Adv. Space Res.*, vol. 55, no. 11, pp. 2641–2656, Jun. 1, 2015.

[7] J. C. Curlander and R. N. McDonough, *Synthetic Aperture Radar: Systems and Signal Processing*. New York, NY, USA: Wiley, 1991.

[8] R. Scharroo *et al.*, "Jason continuity of services: Continuing the Jason altimeter data records as Copernicus Sentinel-6," *Ocean Sci.*, vol. 12, pp. 471–479, 2016, doi: 10.5194/os-12-471-2016.

[9] R. K. Raney, "Milestones in altimeter performance: Past, present, and future with relevance to coastal altimetry," presented at the 8th Coastal Altimetry Workshop, Konstanz, Germany, Oct. 23/24, 2014.

[10] I. G. Cumming and F. H. Wong, *Digital Processing of Synthetic Aperture Radar Data: Algorithms and Implementation*. Boston, MA, USA: Artech House, 2005.

[11] J. L. MacArthur, "Design of the Seasat—A radar altimeter," *Oceans*, vol. 8, pp. 222–229, 1976.

[12] L. Phalippou, L. Rey, and P. de Chateau-Thierry, "Overview of the performances and tracking design of the SIRAL altimeter for the CryoSat mission," in *Proc. Int. Geosci. Remote Sens. Symp.*, Sydney, N.S.W., Australia, 2001, vol. 5, pp. 2025–2027.

[13] W. G. Carrara, R. S. Goodman, and R. M. Majewski, *Spotlight Synthetic Aperture Radar Signal Processing Algorithms*. Boston, MA, USA: Artech House, 1995.

[14] L. M. H. Ulander, H. Hellsten, and G. Stenstrm, "Synthetic-aperture radar processing using fast factorized back-projection," *IEEE Trans. Aerosp. Electron. Syst.*, vol. 39, pp. 760–776, Jul. 2003.

[15] A. Halimi, C. Mailhes, J.-Y. Tourneret, P. Thibaut, and F. Boy, "A semi-analytical model for delay/Doppler altimetry and its estimation algorithm," *IEEE Trans. Geosci. Remote Sens.*, vol. 52, no. 7, pp. 4248–4258, Jul. 2014.

[16] D. J. Wingham *et al.*, "CryoSat: A mission to determine the fluctuations in Earth's land and marine ice fields," *Adv. Space Res.*, vol. 37, no. 4, 2006, pp. 841–871.

[17] G. S. Brown, "The average impulse response of a rough surface and its applications," *IEEE Trans. Antennas Propag.*, vol. 25, no. 1, pp. 67–74, Jan. 1977.

[18] E. S. Garcia, D. T. Sandwell, and W. H. F. Smith, "Retracking CryoSat-2, Envisat and Sentinel-6/Jason-CS-1 radar altimetry waveforms for improved gravity field recovery," *Geophys. J. Int.*, vol. 196, no. 3, pp. 1402–1422, Jan. 2014.

[19] C. Ray *et al.*, "SAR altimeter backscattered waveform model," *IEEE Trans. Geosci. Remote Sens.*, vol. 53, no. 2, pp. 911–919, Feb. 2015.

[20] R. K. Raney, "Maximizing the intrinsic precision of radar altimetric measurements," *IEEE Geosci. Remote Sens. Lett.*, vol. 10, no. 5, pp. 1171–1174, Sep. 2013.

[21] L. Phalippou and F. Demestere, "Optimal re-tracking of SAR altimeter echoes over open ocean: Theory versus results for SIRAL2 data," presented at the OSTST Meeting, San Diego, CA, USA, Oct. 19–21, 2011. [Online]. Available: http://www.aviso. oceanobs.com/fileadmin/documents/OSTST/2011/oral/01_Wednesday/ Splinter\ignorespaces01\ignorespacesIP/02OSTST-2011-Phalippou-Demeestere.pdf

[22] CryoSat Ground Segment Instrument Processing Facility—L1 b Products Specification Format, Advanced Computer Systems, Nov. 14, 2011. [Online]. Available: https://earth.esa.int/documents/10174/125273/[PROD-FMT]_L1_Products_Format_Specification_v4.9.pdf

[23] B. R. Hun, "The application of constrained least squares estimation to image restoration by digital computer," *IEEE Trans. Comput.*, vol. C-22, no. 9, pp. 805–812, Sep. 1973.

[24] M. Studinger, L. Koenig, S. Martin, and J. Sonntag, "Operation IceBridge: Using instrumented aircraft to bridge the observational gap between ICESat and ICESat-2," in *Proc. IEEE IGARSS*, Jul. 25–30, 2010, pp. 1918–1919.

[25] S. W. Laxon *et al.*, "CryoSat-2 estimates of Arctic sea ice thickness and volume," *Geophys. Res. Lett.*, vol. 40, pp. 732–737, 2013.

[26] E. J. Walsh, "Pulse-to-pulse correlation in satellite radar altimeters," *Radio Sci.*, vol. 17, no. 4, pp. 786–800, 1982.

[27] W. H. F. Smith and R. Scharroo, "Waveform aliasing in satellite radar altimetry," *IEEE Trans. Geosci. Remote Sens.*, vol. 53, no. 4, pp. 1671–1682, Apr. 2015.

[28] R. Scharroo, "RADS RDSAR algorithm theoretical basis document version 0.3, CP4O project report," NASA, Washington, DC, USA, 2014. [Online]. Available: http://www.satoc.eu/projects/CP4O/docs/tud _rdsar_atbd.pdf

[29] R. Scharroo, E. W. Leuliette, J. L. Lillibridge, D. Byrne, M. C. Naeije, and G. T. Mitchum, "RADS: Consistent multi-mission products," ESA, Paris, France, Proc. Symp. 20 Years Progr. Radar Altimetry, Spec. Publ., ESA SP-710, 2013.

[30] R. Bamler and M. Eineder, "ScanSAR processing using standard high precision SAR algorithms," *IEEE Trans. Geosci. Remote Sens.*, vol. 34, no. 1, pp. 212–218, Jan. 1996.

Alejandro Egido (S'07–M'13) received the Master's degree in telecommunications engineering (after developing his final research project in the Technical University of Dresden, Dresden, Germany) from the Universidad de Zaragoza, Zaragoza, Spain, in 2007 and the Ph.D. degree in telecommunications engineering from the Polytechnic University of Catalonia, Barcelona, Spain, in 2013.

After his undergraduate studies, he enrolled in an internship at the European Space Agency, where he worked in the Sentinel-1 Copernicus Project. In 2007, he joined Starlab Barcelona, Barcelona, where he worked as a Scientific Researcher. In 2015, he joined the Laboratory for Satellite Altimetry, National Oceanic and Atmospheric Administration (NOAA), College Park, MD, USA, where he is currently working in the development of improved SAR altimetry products and algorithms for physical oceanography and sea ice applications. He is also currently with the Cooperative Institute for Climate and Satellites, University of Maryland, College Park. His main research interests include the use of Global Navigation Satellite System (GNSS) signals as a source of opportunity for remote sensing applications; the Passive Reflectometry and Interferometry System (PARIS) concept; and the use of SAR altimetry for the characterization of open ocean, coastal, and polar zones.

Dr. Egido was a recipient of the Technology Innovation Award from the NOAA National Environmental Satellite, Data, and Information Service (NESDIS) Center for Satellite Applications and Research (STAR) for developing fully focused SAR altimetry in 2016.

Walter H. F. Smith received the B.Sc. degree from the University of Southern California, Los Angeles, CA, USA, in 1984 and the M.A. and Ph.D. degrees from Columbia University, New York, NY, USA, in 1986 and 1990, respectively, all in geological science.

From 1984 to 1990, he was a Graduate Research Assistant with Columbia University. From 1990 to 1992, he was a Cecil and Ida Green Foundation Scholar in the Institute of Geophysics and Planetary Physics, Scripps Institution of Oceanography, La Jolla, CA. Since 1992, he has been a Geophysicist with the National Oceanic and Atmospheric Administration (NOAA), College Park, MD, USA, where he does research on the applications of satellite radar altimeter measurements of sea level to topics as varied as tsunami propagation, hurricane intensification, storm surge, wind speed and wave height, mesoscale ocean currents and eddies, ionosphere electron content, and the mapping of the marine gravity field and related bathymetry. His publications cover these and other topics, including the mapping of the ocean floors, the volcanic history of the ocean basins, and the lubrication of plate tectonics. His papers with D. T. Sandwell applying satellite altimetry to marine gravity and bathymetric estimation are the most cited papers in oceanography. He served on the United Nations Committee for the General Bathymetric Chart of the Oceans for more than 20 years. He was a Principal Investigator on the Altimetric Bathymetry from Surface Slopes ("ABySS") mission proposal for a delay/Doppler radar altimeter mission to map Earth's oceans.

Dr. Smith was a recipient of a U.S. Department of Commerce Gold Medal for scientific breakthroughs in the application of altimetry to bathymetric estimation, a NOAA Administrator's Award for rescuing and reprocessing data from the U.S. Navy Geosat mission, a NOAA Administrator's Award for scientific excellence and leadership in developing near-real-time marine and hurricane forecast system data from the European Space Agency CryoSat-2 mission, and a NESDIS STAR Technology Innovation award for developing fully focused SAR altimetry.